33RD CONGRESS
OF THE INTERNATIONAL COUNCIL
OF THE AERONAUTICAL SCIENCES
STOCKHOLM, SWEDEN, 4-9 SEPTEMBER, 2022

ICAS 2022 SWEDEN

MORPHING FORWARD WING SECTION SKIN DESIGN FOR A SAILPLANE CONSIDERING WING BENDING

Fabian Sturm[1] & Mirko Hornung[1]

[1]Institute of Aircraft Design, Technical University of Munich

Abstract

A sailplane with a morphing forward wing section promises a significant performance increase compared to conventional designs. The morphing skin shall adopt the desired aerodynamic shapes for fast and slow flight, that are imposed by discrete ribs with compliant mechanisms. These shapes shall also be achieved in between those ribs. For high-aspect ratio wings on sailplanes, spanwise bending deformation is significant and the morphing shell must not buckle or fail. Also a low deformation energy for morphing and a low mass are desired. Studies show different results for a quasi-2D jig-shape compared to a wing with increasing spanwise bending, where bending deformations in two directions are superimposed. A modelling and analysis approach is shown that considers these 3D effects. A FEM simulation of a representative wing segment is performed and the resulting elastic airfoil shapes at several flight conditions are analyzed geometrically and aerodynamically. Monolithic shell laminates with balanced ply angles show promising behavior and are chosen as a baseline design. Fiber material, thickness and angle are chosen as design variables for a parameter study for this multi-objective problem. With a stiffness analysis of the laminates, possible correlations between stiffness parameters and objectives are investigated. The optimum skin laminate depends on the chosen objective priorities.

Keywords: morphing structures, variable geometry, composite design, aeroelastic design, airfoil aerodynamics

Nomenclature

Symbols

A	area, mm^2
c_l	lift coefficient, airfoil
C_L	lift coefficient, aircraft
E	Young's modulus, N/mm^2
G	shear modulus, N/mm^2
I	second moment of area, Nmm^4
LE	logarithmic strain, $\mu m/m$
m	mass, kg
n_z	aircraft load factor
p	pressure, N/mm^2
t	thickness, mm
v	airspeed, km/h
V_f	fiber volume fraction
V_A	design maneuver airspeed, km/h
w	width, mm
W	work, J
ν	Poisson ratio
x,y,z	wing coordinate system
$1,2,3$	ply coordinate system

Abbreviations

C	carbon
CM	compliant mechanism
CLT	classical laminate theory
CFRP	carbon fiber reinforced plastics
FEM	finite element method
G	glass
GFRP	glass fiber reinforced plastics
HM	high modulus
HT	high tenacity
PP	polypropylene
PPFRP	polypropylene fiber reinforced plastics
UD	unidirectional
WF	woven fabric

1. Introduction and Motivation

Sailplanes fly at several flight conditions, from circling at low airspeeds in thermals to cruising at high airspeeds. The objective is to maximize the overall speed. Airfoils with hinged trailing edge flaps are state of the art to operate within the laminar-low-drag-bucket over the whole range of lift coefficients. Airfoils with a higher maximum lift coefficient within the laminar-low-drag-bucket allow a reduction of the wing area and therefore reduce profile drag. The aspect ratio is increased at a constant span and with a constant mass the wing loading is also increased. Thus, higher lift to drag ratios can be achieved at higher airspeeds. This can be even enhanced by combining a morphing forward section with a conventional trailing edge flap, which results in a maximum lift coefficient of up to $C_L = 1.8$ [13]. By morphing the forward section, the airfoil shape is switched from low- to high speed configuration during flight. Airfoils and a wing for an 18 m span sailplane with this concept have been designed and numerically optimized by Achleitner et al. [1].

The structural concept of the wing structure is shown in Figure 1. The morphing shell is supported by elastically deformable, discrete ribs. These are composed of compliant mechanisms (CM) that impose a specific target displacement at discrete points along the morphing shell, to achieve the desired airfoil shape. The shape of those CMs is the result of a topology optimization with the objective to achieve a precise output displacement from a given input deflection at the lower side of the shell [8]. On the lower side there is a structural gap in the shell, which allows lateral displacement. It is aerodynamically sealed with a plastic tape, a method that is currently applied for sealing trailing edge flaps. Thus, the leading edge is not rolled up and keeps its shape during morphing and no additional membrane strains are induced. The input deflection is applied mechanically on the lower side of the morphing shell.

The motivation is, to model the wing and to study and design a deformable shell laminate of such a morphing sailplane wing, that fulfills the objective of good aerodynamic performance, structural stability and strength as well as low deformation energy for little actuation work. Due to significant wing bending, 3D effects have to be considered in the model.

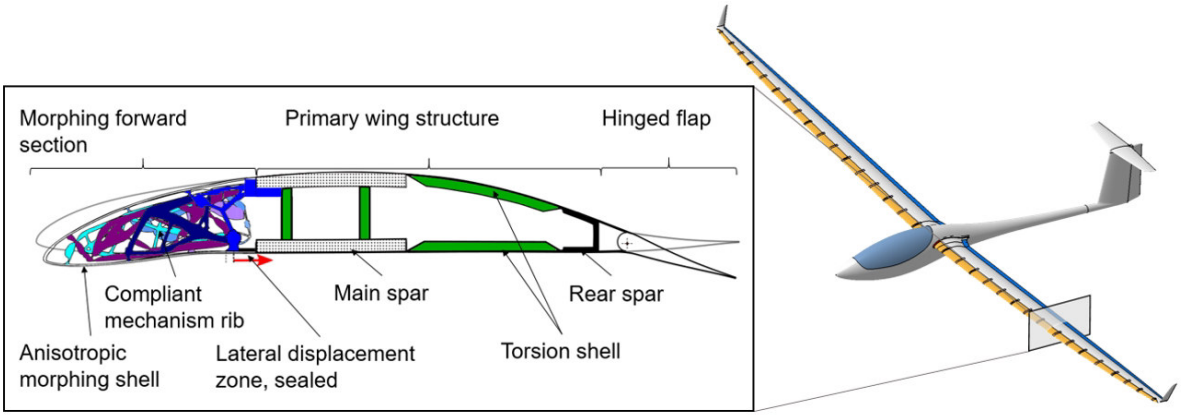

Figure 1 – Structural concept of a sailplane with a morphing forward wing section

2. State of the Art

In contrast to the proposed concept, several concepts can be found that apply a morphing shell that is connected to the front spar both on the upper and lower side which leads to additional membrane strains and a roll-up movement of the nose.

Monner et al. [6] developed a morphing leading edge device for large aircraft which is seamless and gapless to achieve a high-lift device that allows to maintain laminar flow. Based on that, Kintscher et al. [4] further investigated the morphing forward section with a metallic compliant mechanism actuation based on topology optimization and a tailored stiffness skin layup optimization with a 3D wing geometry. As a skin concept a design with a hybrid laminate of GFRP and ethylene propylene diene monomer rubber (EPDM) was investigated.

Rudenko et al. [9] built a structural optimization framework to optimize a hybrid composite skin together with the inner kinematic actuation mechanism. The objective function is a weighted addition

considering curvature, shape and strains. As a result the skin has a high bending stiffness anisotropy. A quasi 2D test specimen is built and compared to the simulations. 3D wing bending and buckling is not shown in the models.
Morishima et al. [7] investigated a morphing forward section for a large aircraft with an internal actuation. The model considers large deformations with geometric nonlinear FEM with a quasi 2D model.
Within the presented project, previous studies have been done. Three different skin design concepts for anisotropic morphing shells have been investigated by Sturm et al. [10]. All concepts have CFRP UD plies in spanwise direction to achieve a maximum bending stiffness anisotropy. These concepts are a monolithic shell with low density polypropylene fiber core plies, a conventional sandwich with a foam core and the CellSkin concept. The latter is comprised of CFRP face sheets and GFRP shear webs, orientated in spanwise direction.
In [11] Sturm presented the requirements more precisely and showed a parameter study on laminate parameters with a stiffness analysis of flat plates with classical laminate theory (CLT) and a FEM-wing model. Due to global wing bending, spanwise strains of the wing's primary structure are imposed on the morphing shell. The upper side of the morphing shell is imposed with compression strain and especially prone to buckling. Also for pure spanwise UD plies, there is little in-plane shear stiffness, so shear buckling can occur. Orienting the fibers as a balanced ply laminate around the spanwise direction shows promising benefits with respect to airfoil shape but requires higher deformation work. However with large wing bending, the effect on deformation work in relation to fiber angle is reversed.

3. Methodology

3.1 Geometry and FE-Model

The model dimensions and boundary conditions are chosen for a 18 m span sailplane that was designed for the application of a morphing forward section. To consider proper boundary conditions for one single cross section within a 3D wing under spanwise bending, an inner wing segment with a spanwise dimension of 2200 mm is modelled. The design chord length is 550 mm with a spanwise rib spacing of 500 mm. A specific morphing airfoil designed by Achleitner is used [1]. The model is shown in Figure 2. Only the forward morphing section (until 0.25 chord) and the box spar are modelled. Between the morphing zone and the spar caps, there is a zone with shell laminate that should not deform during morphing. At each rib location there are six stacked compliant mechanisms, each with a single actuation point. They are distributed along the forward section and are modelled with elastic connectors, connected to the spar as shown on the right side. For the slow flight configuration the vertical target displacement is applied there, to achieve the design airfoil coordinate. A spring stiffness is applied in parallel with the stiffness, measured from a separate compliant mechanism FE-model. To represent the mechanical actuation on the lower skin side, a horizontal target displacement is applied at three spanwise locations between the ribs. This model simplifies the real elastic behavior of the CMs, as not all coupled stiffnesses are modelled. The skin is discretized with shell elements and the nodal coordinates along one cross section are analyzed. The design parameters are chosen from previous experience and considered constant for this study although they have an impact on the overall result. As the FEM-nodal coordinates are used to create 2D-airfoil coordinates, the influence of the shell element size is investigated.

3.2 Wing Deformation

The global wing deformation under aerodynamic and inertia loads of a high-aspect-ratio sailplane wing with a forward morphing section has been investigated and optimized with the objective to reduce twist by Sturm et al. [12]. A FEM wing model with shell elements and a rigid fuselage and tail is coupled with a doublet-lattice-method (DLM) aerodynamic model and a mass model of the aircraft. A static aeroelastic response with linear FEM is calculated for each load case. Based on these results, the local bending curvatures are analyzed by deriving the displacements twice with respect to y. For the inner wing segment, an average curvature is calculated and used as a constant value as shown in Figure 3. This value is then integrated twice along y to get again the corresponding displacement. By this, a constant bending strain condition can be created for the wing cross section.

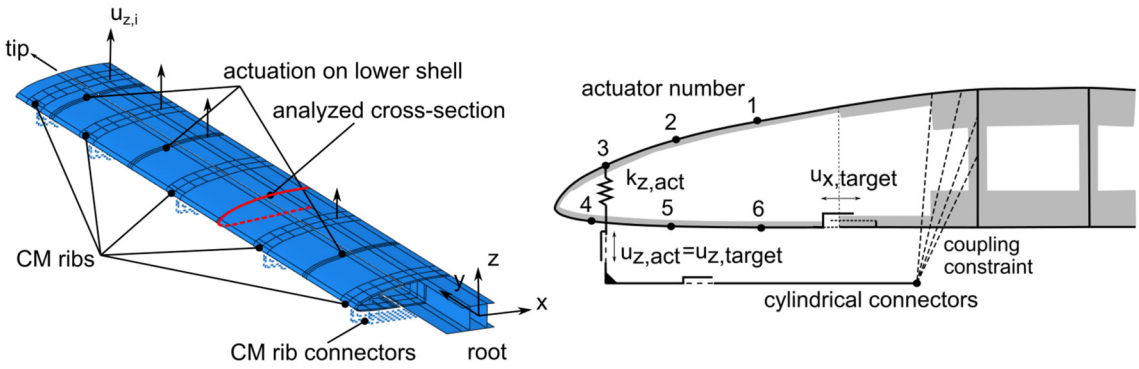

Figure 2 – FEM shell model of morphing forward section (left), CM-rib actuation points with connectors (right)

Table 1 – Load step configurations

Load Step	Description	morph config	n_z $[-]$	V $[km/h]$	C_L $[-]$	p_{up} $[N/mm^2]$	p_{low} $[N/mm^2]$
1	Jig, aero pressure, fast	fast	0.0	0.0	-	4.55E-04	-2.27E-04
2	Jig, aero pressure, slow	slow	0.0	0.0	-	4.55E-04	-2.27E-04
3	Cruise VA, fast, const curv	fast	1.0	220	0.30	4.55E-04	-2.27E-04
4	Thermaling, fast, const curv	fast	1.3	118	1.35	5.91E-04	-2.96E-04
5	Thermaling, slow, const curv	slow	1.3	110	1.55	5.91E-04	-2.96E-04
6	Maneuver $n_z = 2$, fast, const curv	fast	2.0	150	1.28	9.09E-04	-4.55E-04
7	Maneuver $n_z = 2$, slow, const curv	slow	2.0	150	1.28	9.09E-04	-4.55E-04
8	Maneuver $n_z = 3$, fast, const curv	fast	3.0	185	1.26	1.36E-03	-6.82E-04
9	Maneuver $n\_z = 3$, slow, const curv	slow	3.0	185	1.26	1.36E-03	-6.82E-04
10	Pull-up V_A, fast, const curv	fast	5.3	238	1.35	2.41E-03	-1.20E-03
11	Pull-up V_A, slow, const curv	slow	5.3	220	1.58	2.41E-03	-1.20E-03

These displacements are applied on the spar. To represent relevant flight conditions, a number of load cases for a 18 m span sailplane with a mass of $m = 600kg$ is investigated as listed in Table 1. They represent jig-shape $(n_z = 0)$, horizontal cruise flight $(n_z = 1)$, circling flight $(n_z = 1.3)$ and maneuver load cases up to an aircraft load factor of $(n_z = 5.3)$. For each case, the airfoil shape is switched between fast flight and slow flight configuration. By regarding both fast and slow flight configurations at one global load factor, its influence on the results can by studied. An averaged constant aerodynamic pressure is applied on the upper and lower side of the morphing shells. The model is clamped in the root area and supported in x-direction on the aft part of the spar to prevent displacements in this direction as well as spanwise twist.

3.3 Morphing Skin Laminates

In total, 16 different laminates are investigated. They are listed with their names and layups in Table 3. The discrete balanced ply angle, the fiber material (high-tenacity carbon-fiber or glass-fiber) and a discrete selection of core thicknesses are design variables. To keep the number of variants low, only three fiber angles are investigated. They represent the extremes of directional stiffness and one intermediate value. The elastic properties of the fiber composite materials are listed in Table 2. To study the general influence of laminate stiffness on the results, four monolithic laminates with six woven fabric (WF) plies and a constant fiber angle are investigated. All other laminates are modelled as monolithic shells with two low density polypropylene (PP) core plies and balanced unidirectional (UD) plies. A GFRP WF ply on top shall act as a crack stopper and base for a paint layer. The reference axis is the spanwise direction of the wing. A cross section with the actual ply thicknesses of one exemplary laminate is shown in Figure 4. In the model, a number of discrete laminate zones can

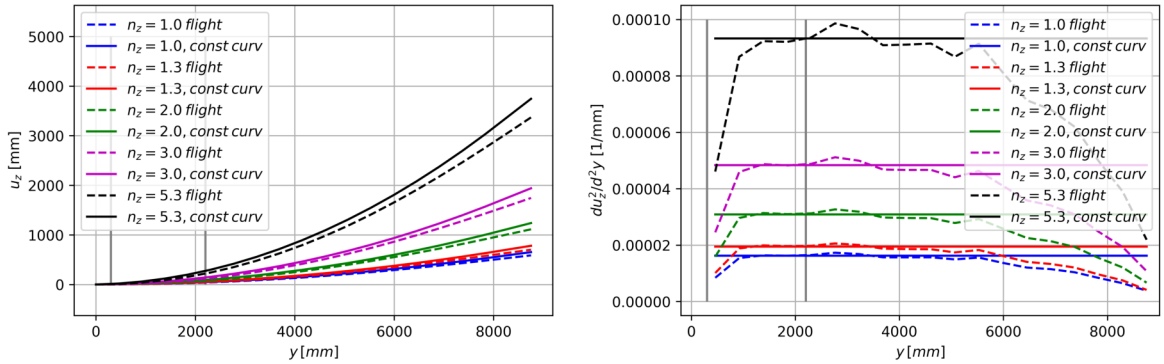

Figure 3 – Bending displacements (left) adapted for constant curvature (right) in inner wing area until $y = 2100mm$

Table 2 – Fiber composite materials elastic properties

Material	$V_f[-]$	$E_1[MPa]$	$E_2[MPa]$	$\nu_{12}[-]$	$G_{12}[MPa]$	$G_{13}[MPa]$	$G_{23}[MPa]$
GFRP E UD	0.5	38100	9927	0.285	3941	3941	3490
CFRP HT UD	0.5	116600	9106	0.290	4024	4024	2957
Innegra S WF	0.5	3927	3927	0.200	839	839	839
GFRP E WF	0.5	23143	23143	0.150	5286	5286	5286
CFRP HT WF	0.5	56386	56386	0.037	2314	2314	2314

be defined along the curve length of the morphing section. Within the scope of this study, all laminate zones are equal to reduce the number of design variables. Only one example named $C-30-zones$, has a combination of two laminates in the cross-section. For manufacturing reasons, the lower and upper shell are bonded at the nose, so there is an overlapping zone with a higher thickness.

3.4 Analysis Procedure

The analysis procedure comprises several steps as shown in the flowchart in Figure 5. The geometries of the design airfoils for both configurations and wing planform geometry are processed to generate a 3D wing geometry with all relevant spatial coordinates. Also a 3D surface CAD model is automatically created. The target displacements between the two airfoil configurations are calculated and used as an input for FEM. With that, a FEM shell model is automatically created within Abaqus CAE using a Python script. A geometric non-linear analysis is performed with Abaqus CAE for all relevant load cases. The resulting node coordinates in one cross section are analyzed, processed and transformed based on the initial geometry model. As the aft part of the wing is not modelled, the design airfoil coordinates are added to the deformed forward part. With transformation and scaling operations, normalized 2D airfoil coordinates are created with a B-spline representation, which are then re-panelled and analyzed with the 2D aerodynamic panel software XFOIL [3]. As the airfoil shape is now depending on the aircraft load case, an automated geometry and aerodynamic analysis is performed for each one, which results in lift and drag polars. Buckling can be identified visually or implicitly due to a significant decay in aerodynamic performance. The total elastic energy within the morphing forward section is measured from the FEM response to compare the required deformation work. Laminate stresses and strains along the cross-section are analyzed as well. The laminate design variables can be updated within the procedure, to study the impact on the objectives. In parallel, the elastic properties of the laminates are analyzed with CLT [5]. From the FEM simulation the ply strains (LE) over the whole laminate envelope and the maximum stress criterion values (MSTRS) of the analyzed cross-section are exported [2].

The objectives are to minimize the required elastic work W_{el} for morphing and to achieve drag coefficients not higher than those of the design airfoils for the cruise and circling cases within the range of the laminar-low-drag-bucket. Also the maximum lift coefficients shall be reached. Buckling must not

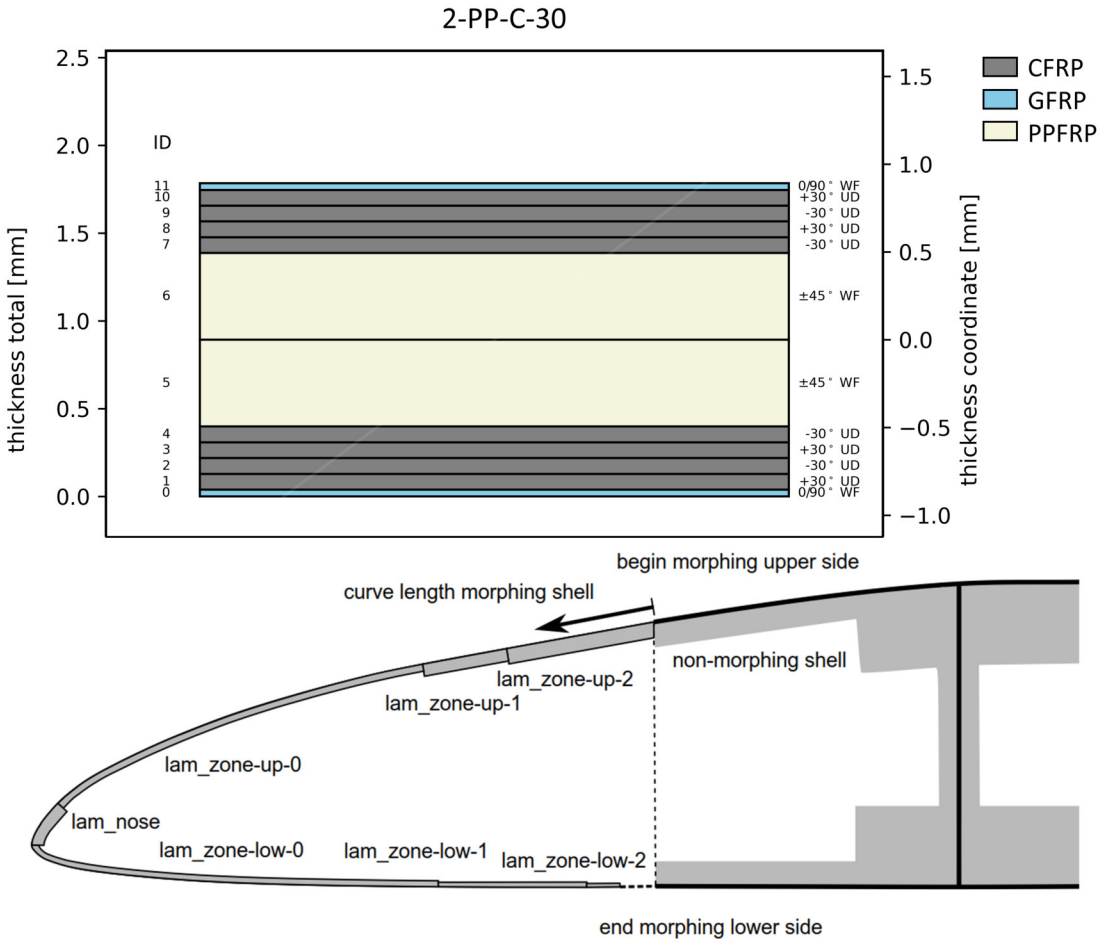

Figure 4 – Laminate zones in cross section with example layup for $\pm 30^\circ$ CFRP UD with two layers of PPFRP

occur up to limit load at the pull-up case with $n_z = 5.3$. Maximum stresses and strains in the laminate shall be below the material limits. The mass of the skin shall also be minimized. Available design variables are the balanced ply fiber angle, discrete ply thickness of available materials and the fiber types carbon-fiber (CF) and glass-fiber (GF).

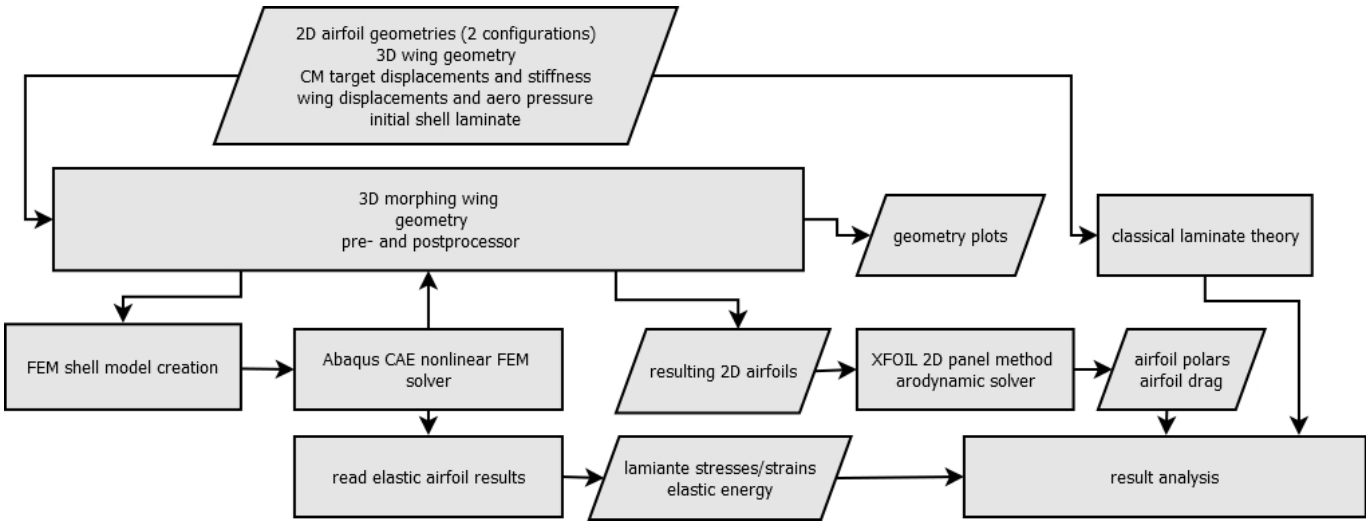

Figure 5 – Flowchart of morphing skin analysis procedure

Table 3 – Laminate names with layups

Name	Layup $(angle_{count}^{fiber\,mat.} - type - area\,weight[g/m^2])$
WF-G-45	$(45_3^G - WF - 280)_S$
WF-G-0/90	$((0/90)_3^G - WF - 280)_S$
WF-C-45	$(45_3^C - WF - 245)_S$
WF-C-0/90	$((0/90)_3^C - WF - 245)_S$
1-PP-G-0	$(45^G - WF - 49/0_4^G - 110/\overline{45^{PP} - WF - 200})_S$
1-PP-G-30	$((0/90)^G - WF - 49/+30^G - 110/-30^G - 110/+30^G - 110/-30^G - 110/\overline{45^{PP} - WF - 200})_S$
1-PP-G-45	$((0/90)^G - WF - 49/+45^G - 110/-45^G - 110/+45^G - 110/-45^G - 110/\overline{45^{PP} - WF - 200})_S$
1-PP-C-0	$(45^G - WF - 49/0_4^C - 80/\overline{45^{PP} - WF - 200})_S$
1-PP-C-30	$((0/90)^G - WF - 49/+30^C - 80/-30^C - 80/+30^C - 80/-30^C - 80/\overline{45^{PP} - WF - 200})_S$
1-PP-C-45	$((0/90)^G - WF - 49/+45^C - 80/-45^C - 80/+45^C - 80/-45^C - 80/\overline{45^{PP} - WF - 200})_S$
2-PP-G-0	$(45^G - WF - 49/0_4^G - 110/45^{PP} - WF - 200)_S$
2-PP-G-30	$((0/90)^G - WF - 49/+30^G - 110/-30^G - 110/+30^G - 110/-30^G - 110/45^{PP} - WF - 200)_S$
2-PP-G-45	$((0/90)^G - WF - 49/+45^G - 110/-45^G - 110/+45^G - 110/-45^G - 110/45^{PP} - WF - 200)_S$
2-PP-C-0	$(45^G - WF - 49/0_4^C - 80/45^{PP} - WF - 200)_S$
2-PP-C-30	$((0/90)^G - WF - 49/+30^C - 80/-30^C - 80/+30^C - 80/-30^C - 80/45^{PP} - WF - 200)_S$
2-PP-C-45	$((0/90)^G - WF - 49/+45^C - 80/-45^C - 80/+45^C - 80/-45^C - 80/45^{PP} - WF - 200)_S$

4. Results

First a mesh convergence study of the FE-model is done. From the FEM simulation of each laminate, the elastic work is extracted. Also the stiffness values of each laminate are analyzed in combination with elastic work to identify design variables that have a significant influence on the results. The geometry of one cross-section of the wing is analyzed with regard to aerodynamic performance. Strains within the laminate are analyzed over curve length of the cross section. The maximum stress criterion is applied to check the structural margin of the laminates.

4.1 FEM-Model Mesh Study

A modelling study with varying element size of the FEM mesh shows two tendencies. The elastic results do not change significantly with element size ($2.5\,mm$, $5.0\,mm$, $7.5\,mm$). However the nodal distance in the nose area has an impact on the accuracy of the airfoil in aerodynamic analysis. Inaccuracies can lead to suction peaks at the nose. Only for the $2.5\,mm$ mesh, there is no significant difference in pressure distribution compared to the design airfoil.

4.2 Elastic Work and Stiffness

In Figure 6 on the left, the elastic work to morph between fast flight airfoil and slow flight airfoil are plotted for all laminates angles and for three load cases. For all laminates the elastic work increases with increasing wing bending. Within each design, the higher the fiber angle, the lower is the increase of work. At $n_z = 0$, the elastic work increases with increasing fiber angle for all laminates, as the chordwise bending stiffness increases. At $n_z = 3.0$ however, the required work for laminates with the same number of PP-plies and the same fiber material stays in the same order of magnitude for all fiber angles. The effect of a thicker laminate with two layers of PPFRP and the stiffer C-fibers compared to G-fibers on the elastic work for morphing can be observed. Additionally, in case of visible buckling below $n_z = 5.3$, the laminate is marked with a red cross. This is the case for all laminates with a fiber angle of 0°. The lowest elastic work is required for laminates with one PP-ply and glass fibers. Two of these variants also don't buckle. The elastic work for $n_z = 5.3$ is not shown, as the values are only available in case of no buckling.

In Figure 6 on the right the two bending stiffness values per unit width for spanwise (around x-axis) and chordwise direction (around y-axis) are shown for all laminates. The orthotropic behavior of the WF laminates and those with 45° fiber angle can be seen. On the other hand, those laminates with 0° UD fiber angle have a high bending stiffness anisotropy. All laminates with either 0° UD fiber angle or

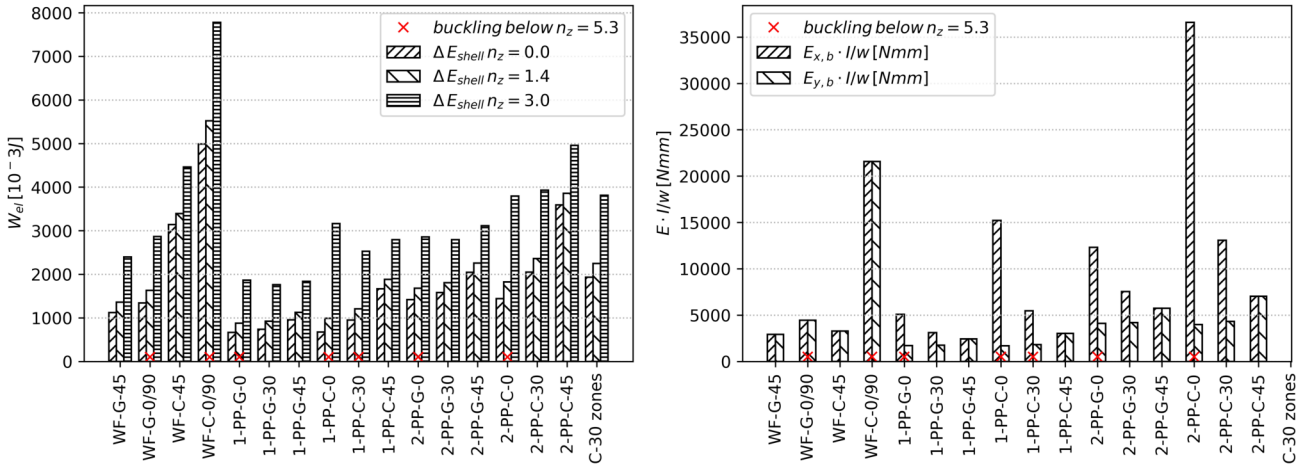

Figure 6 – Elastic work for morphing from fast flight to slow flight configuration at different load cases (left). Bending stiffness per unit width values in spanwise and chordwise direction (right)

0/90° WF buckle below $n_z = 5.3$, although some of them have the highest absolute bending stiffnesses in spanwise direction. For the variant with different laminate zones, no values can be displayed.
In Figure 7 on the left the shear stiffness values per unit width for all laminates are plotted. It can be seen, that those laminates with 45° fiber angle show the highest shear stiffnesses within their designs. The effect is significantly higher for C-fibers compared to G-fibers. All laminates that buckle below $n_z = 5.3$ have comparably low shear stiffness values. There is however one laminate (1-PP-C-30) that buckles, despite having a comparably high shear stiffness.

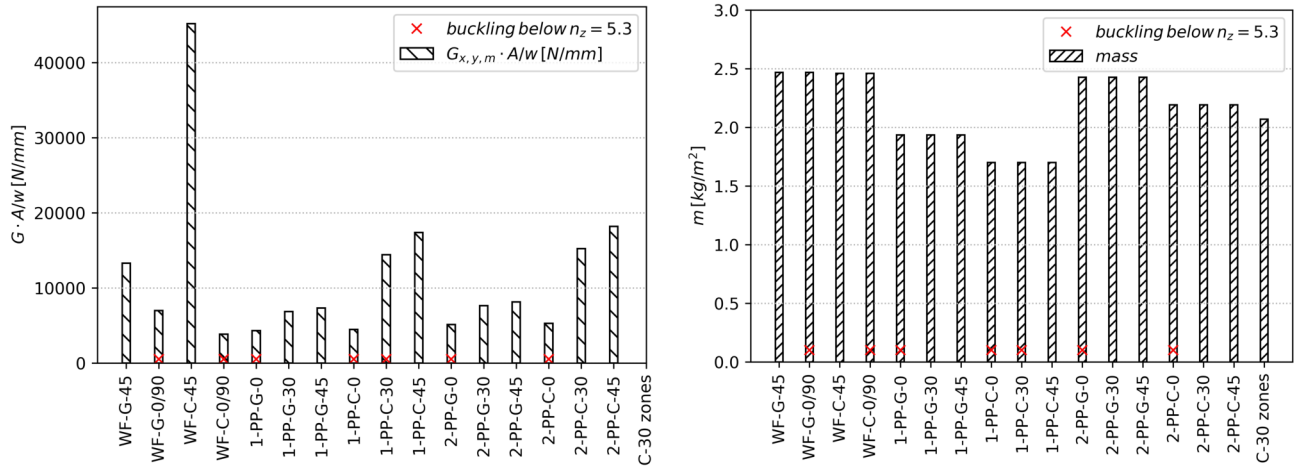

Figure 7 – Shear stiffness per unit width values (left), mass per area (right)

In Figure 7 on the right the mass per area for each laminate is shown. The mass per area for the WF laminates has been chosen to be in the same order of magnitude. The advantage of the sandwich-like behavior of the low density PP-core plies can be seen. For the same thickness, the laminates with G-fibers have a higher mass per area compared to those with C-fibers. With the approach of using different laminates in different zones along the cross section, the mass can potentially be reduced.
To get a more general design guideline for the required laminate stiffness properties, the elastic work for morphing at two load cases ($n_z = 0.0$ and $n_z = 3.0$) is plotted over all five stiffness values per unit width. The results are plotted in Figure 8. Only bending stiffness in chordwise direction shows a visible correlation with elastic work for morphing. This is not the case for all other stiffness properties. The buckling cases are plotted over shear stiffness on the lower right side. All buckling cases show low shear stiffness values, except for one. So, there is no clear upper boundary value where buckling

does not occur. The assumption is, that there is a combination of properties that minimizes elastic work and also prevents buckling.

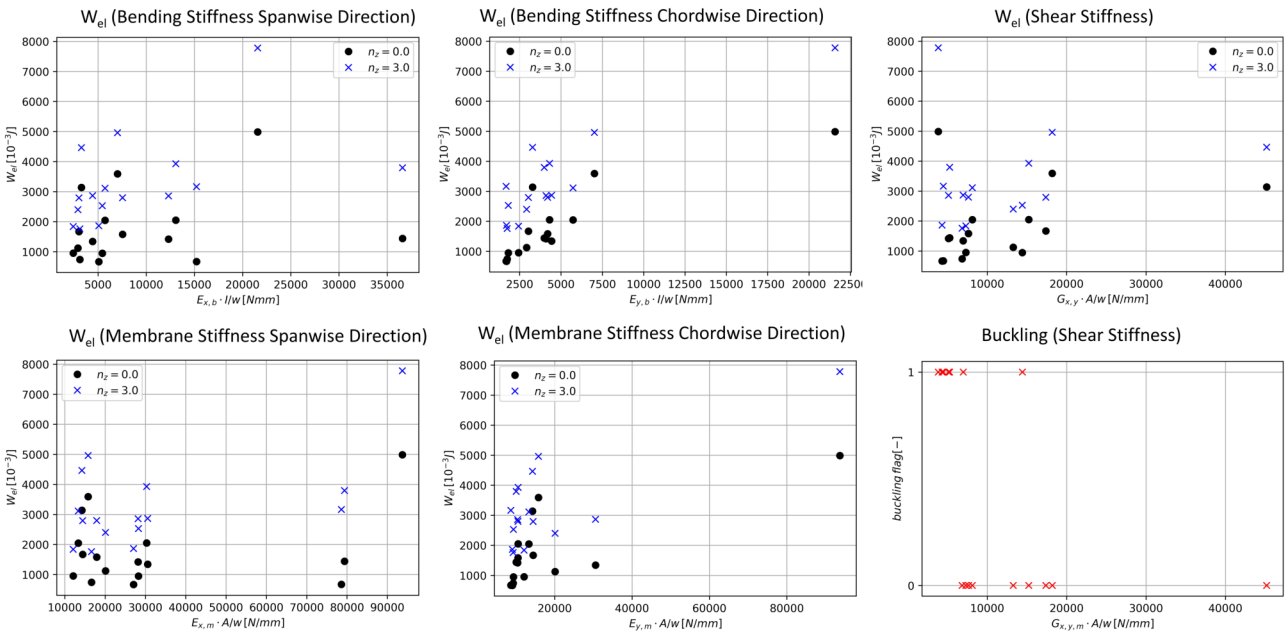

Figure 8 – Delta elastic energies for morphing from fast flight to slow flight configuration at different load cases

4.3 Geometric and Aerodynamic Analysis

For each model, one cross section at $y = 1050\,mm$ is analyzed by extracting the nodal coordinates from the FEM simulation. This location is in between two CM-ribs, so the skin is not supported directly.
In Figure 9 the resulting airfoil geometries and the first derivative of the B-spline curve are plotted of two exemplary laminates. For the aft part, that has not been modelled in FEM, the original design airfoil coordinates are considered.
In the left half, the results of the fast flight configuration are shown. For all airfoils there is small step in the derivative on the lower side compared to the design airfoil. For both laminates there is a larger curvature change on the upper side and a small kink on the lower side at $n_z = 1.0$. This effect vanishes for the 2-PP-C-30 laminate with higher wing bending. For the 2-PP-C-0 laminate a local maximum of the derivative exists on the upper side at $n_z = 5.3$, which does not occur for the 2-PP-C-30 laminate. This correlates with visible buckling of the shell.
In the right half of Figure 9 the results of the slow flight configuration are shown. Already the design airfoil has a step in the derivative and a wavy curve of the lower side, while the upper side is continuous. For all airfoils there is small kink in the derivative on the upper side in the transition area of the morphing zone and the elastic shell in front of the spar. This effect is more distinct for the 2-PP-C-0 laminate. Also the waviness in the derivative on the lower side is no longer there. For the 2-PP-C-0 laminate there still is buckling in the slow flight configuration.
In general the resulting geometries of all laminates look similar. Laminates with 45° fiber angle have the least curvature deviation from the design airfoils.
With these airfoils, a viscous aerodynamic analysis is performed with XFOIL at the two design Re-numbers scaled with $1/\sqrt{c_l}$ for fast flight and slow flight. Although each load case corresponds to a specific lift-coefficient, a whole angle-of-attack sweep is calculated to create lift and drag polars for comparison with the design airfoil. Also, wing bending is influenced mostly by the aircraft load factor which can be reached at different airspeeds and lift coefficients.
In Figure 10 the airfoil polars are plotted. For four load cases, the resulting polars of all laminates are plotted in grey to show the whole variety. The polars of the design airfoils are plotted with a solid black line for fast flight configuration and with dashed line for the slow flight configuration. For

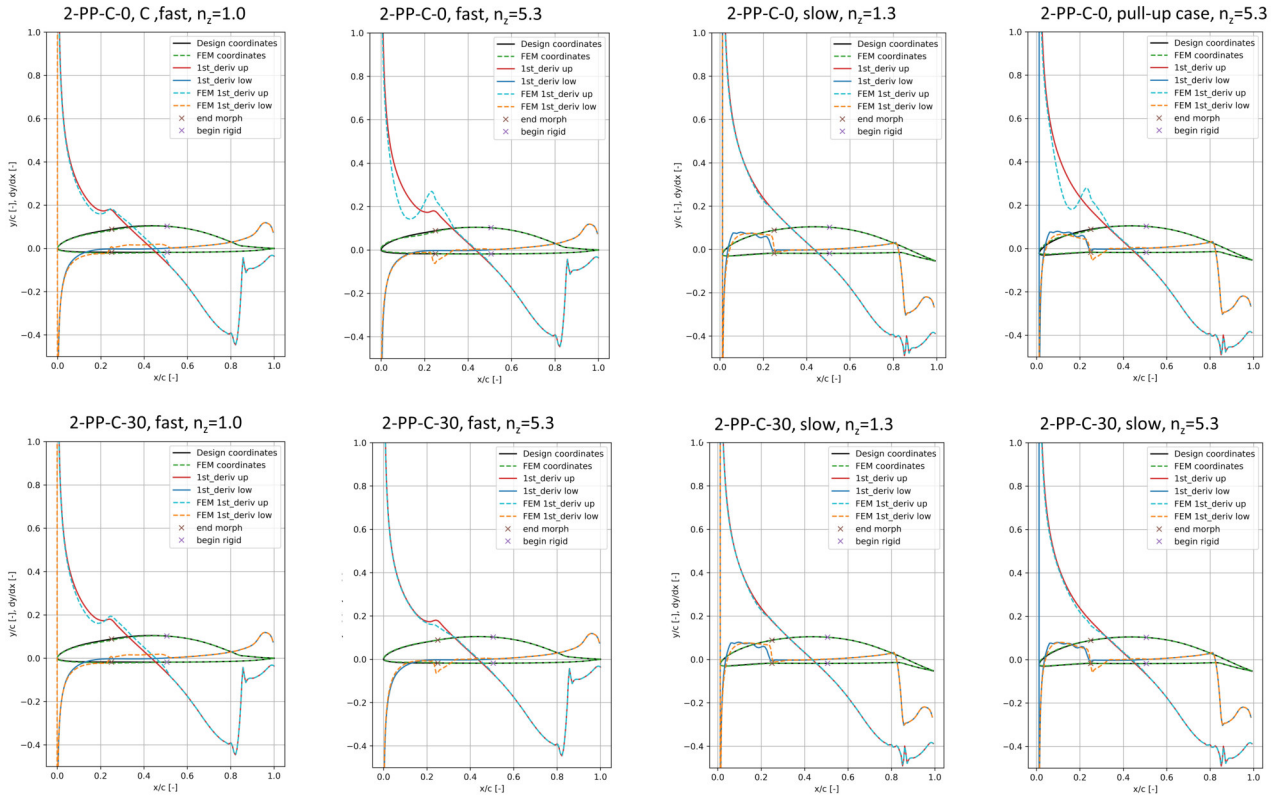

Figure 9 – Airfoil geometries and first derivatives of laminates 2-PP-C-0 and 2-PP-C-30

jig-shape $n_z = 0.0$ with aerodynamic pressure, the drag and lift polars of the elastic airfoils are not visible in fast flight configuration as they match the design airfoil. In slow flight configuration the maximum lift coefficient and the upper corner of the laminar-low-drag-bucket of the elastic airfoils are slightly lower than those of the design airfoil. Some airfoils show a slightly elevated lower end of the laminar-low-drag-bucket. For $n_z = 1.0$ there is only little wing bending, although this has an effect on the airfoil geometries. Depending on the laminate, the kink on the upper side of the airfoils is more distinct than for the design airfoil. This leads to an earlier laminar-turbulent transition and the upper corner of the laminar-low-drag-bucket is at a lower lift coefficient. The lift polars match however. There is no correlation to a specific fiber angle or stiffness parameter of the laminate. For higher wing bending at $n_z = 1.3$ the kink on the upper side of the airfoils for all laminates is reduced again and the deviation of the laminar-low-drag-bucket in fast flight configuration is very small compared to the design. In this circling flight condition the slow flight configuration also shows no significant disadvantage compared to the design airfoil for all laminates. For the pull-up maneuver case at $n_z = 5.3$ drag is no longer relevant, however laminates that buckle can be clearly identified in the drag polars as the drag increases significantly. The range of lift coefficients within the laminar-low-drag-bucket is shifted slightly as the airfoil nose is moved out of position. Within the laminar-low-drag-bucket the desired low drag coefficient of the design airfoils can be reached.

4.4 Strain and Maximum Stress Analysis

The superimposition of morphing and spanwise wing bending also leads to a superimposed strain condition. For understanding the phenomena the laminate WF-C-0/90 is analyzed and the strains for three load cases are shown in Figure 11. In this case the ply directions match the global wing coordinate system. Ply direction 1 corresponds to spanwise direction and ply direction 2 corresponds to chordwise direction. The plot shows the absolute maximum and minimum values of all plies (envelope) along the curve length of the morphing forward section. It starts on the upper side on the left and reaches to the lower side on the right. The relative laminate thicknesses of the zones at this location are plotted on the bottom.

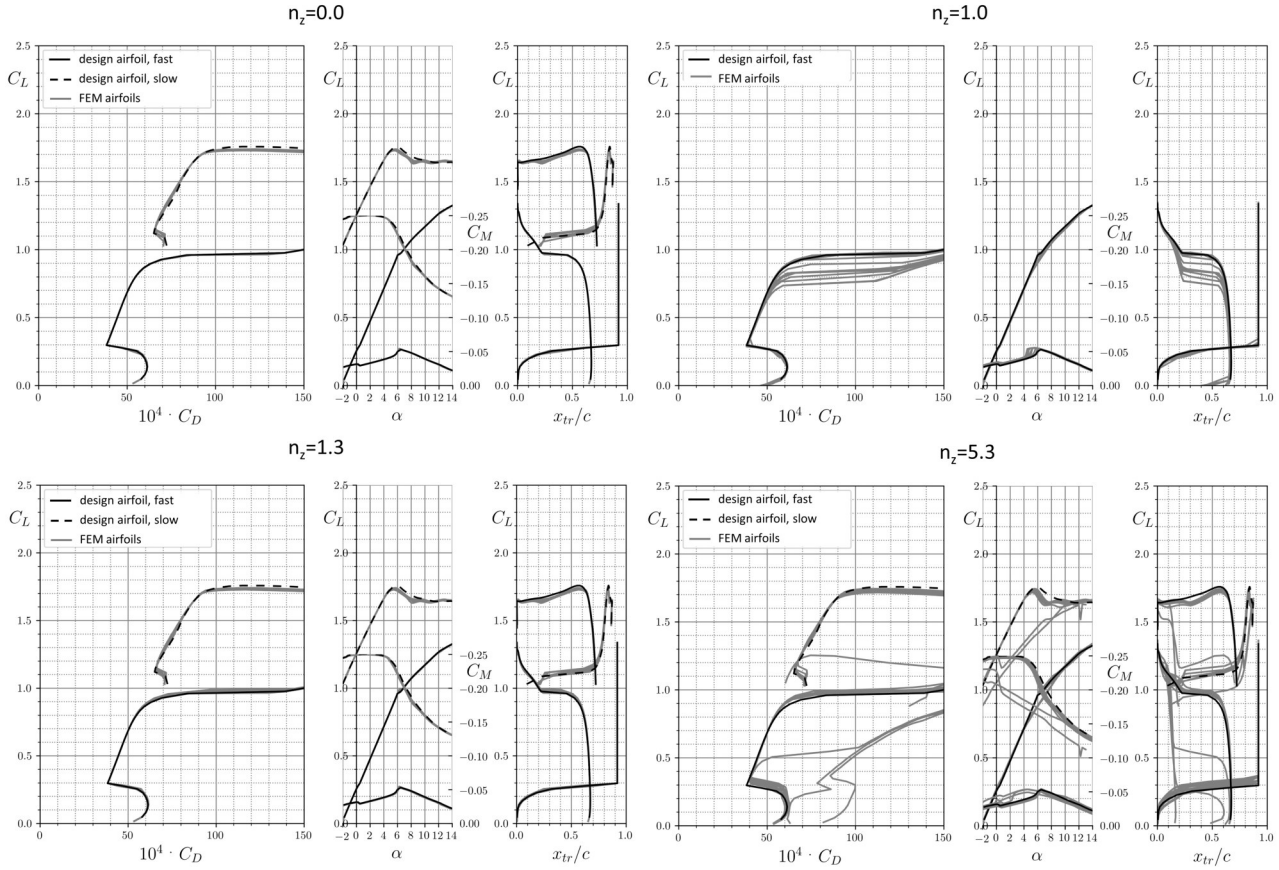

Figure 10 – Airfoil polars

For jig-shape $n_z = 0.0$ with aerodynamic pressure there is no significant strain in the laminate. In slow flight configuration a pure bending strain in chordwise direction can be seen with positive and negative values. The maximum values are reached at the beginning of the morphing area on the upper side. The nose is almost unloaded and on the lower side the bending strain reduces to zero towards the structural gap.
For $n_z = 1.3$ there is wing bending. In fast flight configuration (no morphing) there is a compression strain (negative values) on the upper side that crosses zero before the nose. On the lower side there is tension strain (positive values). Shear strain increases towards the nose, however within the nose laminate the values are locally lower. On the right side the superimposition of strains can be seen.
For $n_z = 5.3$ with significant wing bending the strain values from bending are already higher than those of morphing at $n_z = 0.0$, as there is already bending strain in the laminate without morphing, which indicates that the forward section is forced to keep its shape during this case. Spanwise bending strain and shear strain are increased. For the slow flight configuration the strain value for shear increases significantly at the upper beginning of the morphing section. The value varies significantly along the upper side.
It can be seen that wing bending has a significant effect on the strain within the skin laminate. The interpretation of strain effects for laminates with rotated fiber direction is no longer intuitive, as the strains are no longer corresponding to the wing coordinate system.
In Figure 12 the maximum stress criterion value (MSTRS) over all plies in the cross section is displayed for the laminate named $C-30-zones$. Here, the laminate 2-PP-C-30 is used on the upper side and on the forward part the lower side. Towards the gap on the lower side the laminate 1-PP-C-30 is used. In addition to the MSTRS value, for every fifth element, the ply ID number of the highest MSTRS value is plotted. The laminate 2-PP-C-30 cross section is also shown in Figure 4. For slow flight configuration at $n_z = 0.0$ the outer plies ID 11 and ID 0 have the highest MSTRS values from

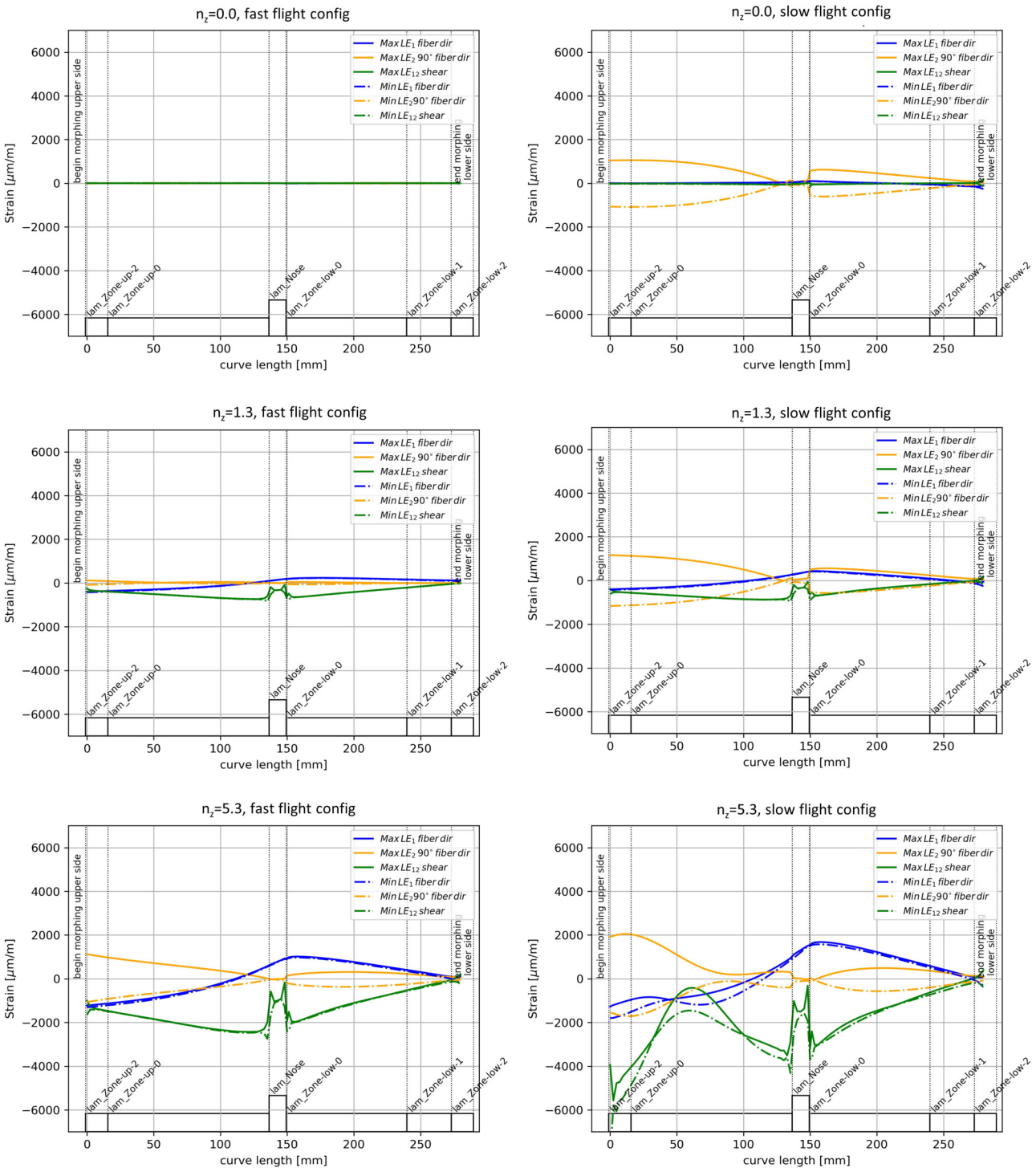

Figure 11 – Maximum LE strain values per element (envelope over all plies) WF-C-0/90

pure bending. This is also the case for $n_z = 1.3$. For bending in fast flight configuration at $n_z = 1.3$ the UD C-fibers with IDs 1, 2 and 9 are loaded most. This is also the case for $n_z = 5.3$. In slow flight configuration some parts of the laminate are highest loaded from bending, other parts from morphing. In general the MSTRS value is higher in the thinner laminate 1-PP-C-30, but this can be tolerated on the lower side as the stress level is low there.
In general the MSTRS values for all laminates are below the critical value of 1.0 for all load cases in this cross section.

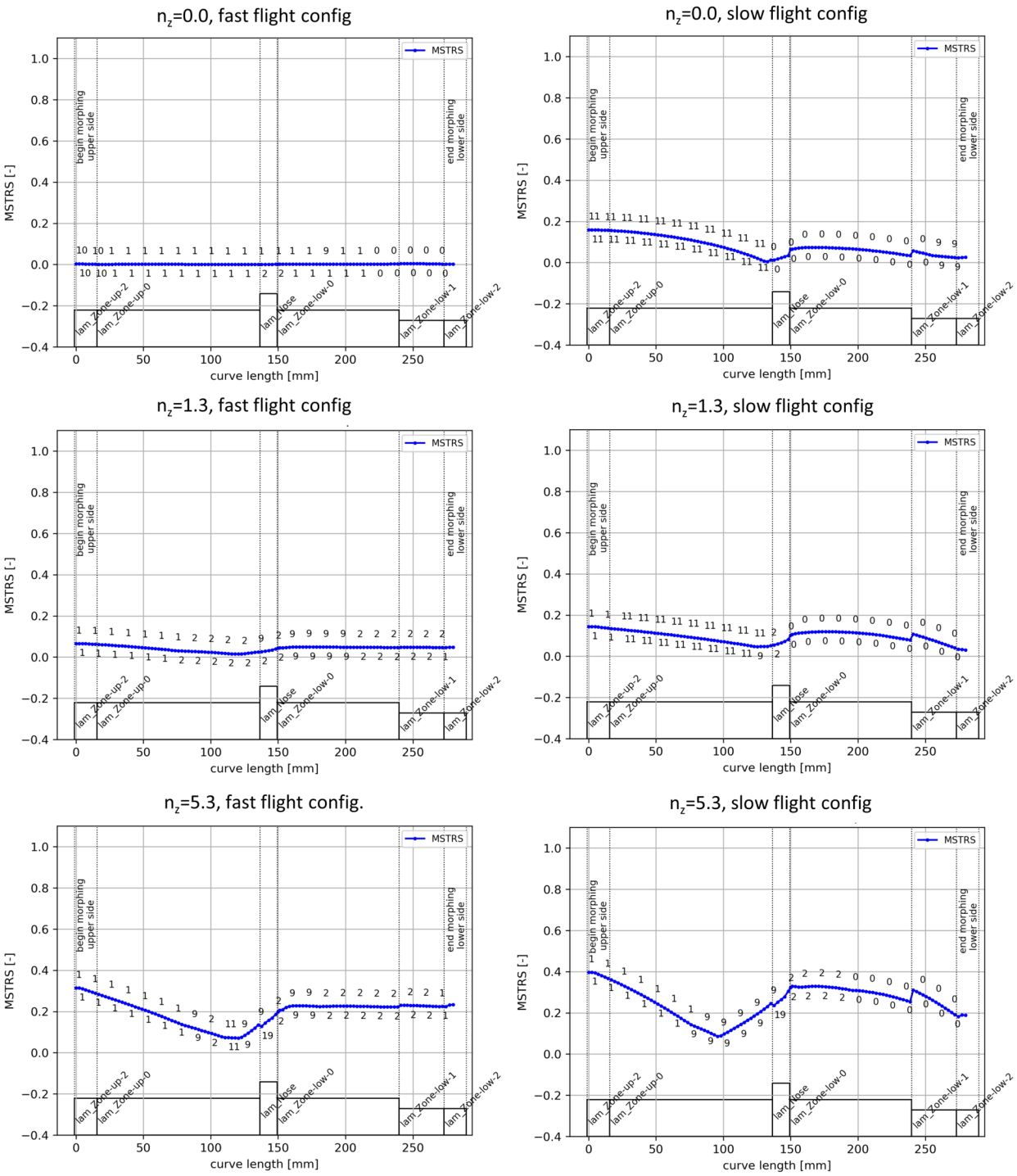

Figure 12 – Maximum stress criterion value per element (envelope over all plies) C-30-zones (1-PP-C-30 and 2-PP-C-30)

5. Conclusion and Outlook

A modelling and analysis approach is presented to simulate the effect of wing bending on a morphing forward wing section. Structural and aerodynamic analysis is performed on the resulting cross-section geometry for several load cases. A balanced ply laminate is investigated for several layups. First results showed a beneficial effect of this laminate design on shape and aerodynamic performance compared to fibers aligned in spanwise direction.

The skin laminates require varying elastic work for morphing, depending on their layup and the wing bending load case. Laminates with a low chordwise bending stiffness require the least elastic work

for morphing. However, to prevent buckling below $n_z = 5.3$, a minimum shear stiffness is required as all laminates with only spanwise fiber orientation buckle. There is one laminate though that buckles, despite a higher shear stiffness. A high bending stiffness anisotropy does not prove to be an advantage. Further investigations shall be done, to find an optimum set of stiffness parameters and to select laminate parameters from that. Although laminates with glass fibers require less elastic work, they have a higher mass, compared to carbon fiber laminates.
The geometry deviations of all laminates are small for the cruise and circling flight load cases, so the desired aerodynamic performance can be achieved. Some laminates however show a lower upper corner of the laminar-low-drag-bucket at $n_z = 1.0$. Also, if a laminate buckles, the aerodynamic performance is significantly reduced.
A superimposition of strains from wing bending and chordwise morphing can be seen. The influence of wing bending on the strain values and the maximum stress criterion is significant. In jig-shape at $n_z = 0.0$, morphing leads only to small strains. In general the stress and strain levels for all laminates are low enough to be acceptable.
Considering the objectives and the set constraints, laminates with a balanced fiber angle of 30° or higher, a PP-core and either carbon- or glass fibers can be used for the application of a morphing forward section. The result depends on the chosen objective priorities. By combining different laminates in chordwise zones on the upper and lower side, further advantages in mass and stiffness can be utilized. The effect of a more detailed CM rib model on the results shall be investigated. Also, the influence of other geometric and stiffness parameters on the results can be further investigated.

6. Acknowledgment

The present studies have been funded under the grant of the German federal aviation research program LuFo V-3 (Luftfahrtforschungsprogramm V-3). The authors would like to acknowledge the support of the German Federal Ministry for Economic Affairs and Climate Action.

7. Contact Author Email Address

To contact the author, please mail to: fabian.sturm@tum.de

8. Copyright Statement

References

[1] Achleitner, J., Rohde-Brandenburger, K., Rogalla von Bieberstein, P., Sturm, F., and Hornung, M. Aerodynamic Design of a Morphing Wing Sailplane. In *AIAA Aviation 2019 Forum*, page 4, Reston, Virginia, 06172019. American Institute of Aeronautics and Astronautics.

[2] Dassault Systemes. Simulia user assistance 2018: Abaqus analysis guide.

[3] Drela M. XFOIL: An analysis and design system for low reynolds number airfoils. 1989.

[4] Kintscher M., Monner, H. P., Vasista S., and Rudenko A. Multifunctional skin material for morphing leading edge applications. In *20th International Conference on Composite Materials*, 2015.

[5] MIL-HDBK-17-3F. Composite materials handbook: Volume 3. polymer matrix composites maerials usage, design, and analysis, 2002.

[6] Monner, H. P., Kintscher M., Lorkowski, T., and Storm, S. Design of a smart droop nose as leading edge high lift system for transportation aircrafts. In *50th AIAA/ASME/ASCE/AHS/ASC Structures 2009*, page 3.

[7] Morishima R., Guo S., and Ahmed S. A composite wing structure with a morphing leading edge. In *51st AIAA/ASME/ASCE/AHS/ASC Structures, Structural Dynamics, and Materials Conference; 18th AIAA/ASME/AHS Adaptive Structures Conference*, page 297, Reston, Virigina, 2010. American Institute of Aeronautics and Astronautics.

[8] Reinisch J., Wehrle E., and Achleitner, J. Multiresolution Topology Optimization of Large-Deformation Path-Generation Compliant Mechanisms with Stress Constraints. *Applied Sciences*, 11(6):2479, 2021.

[9] Rudenko A., Hannig A., Monner, H. P., and Horst P. Extremely deformable morphing leading edge: Optimization, design and structural testing. *Journal of Intelligent Material Systems and Structures*, 29(5):764–773, 2018.

[10] Sturm F., Achleitner J., Jocham K., and Hornung M. Studies of anisotropic wing shell concepts for a sailplane with a morphing forward wing section. In *AIAA Aviation 2019 Forum*, page 4, Reston, Virginia, 06172019. American Institute of Aeronautics and Astronautics.

[11] Sturm F. and Hornung M. Morphing shell design of a sailplane with a morphing forward wing section. In *XXXV OSTIV Congress – Congress Program and Proceedings, TU Braunschweig – Niedersächsisches Forschungszentrum für Luftfahrt*, 2021.

[12] Sturm F., Illenberger G., Techmer D., and Hornung M. Static aeroelastic tailoring of a high-aspect-ratio-wing for a sailplane with a forward morphing wing section. In *32nd Congress of the International Council of the Aeroanautical Sciences, Deutsche Gesellschaft für Luft- und Raumfahrt*, 2021.

[13] Weinzierl M., Achleitner, J., and Baier H. Highly extensible skin of a variable geometry wing leading edge of a high-performance sailplane. *Technical Soaring*, (Vol. 39, No. 1):4–9, 2015.